Optics and Lasers in Engineering 65 (2015) 73–80

Contents lists available at ScienceDirect

Optics and Lasers in Engineering

journal homepage: www.elsevier.com/locate/optlaseng

High-efficiency and high-accuracy digital image correlation for three-dimensional measurement

Yue Gao, Teng Cheng*, Yong Su, Xiaohai Xu, Yong Zhang, Qingchuan Zhang*

CAS Key Laboratory of Mechanical Behavior and Design of Materials, Department of Modern Mechanics, University of Science and Technology of China, Hefei 230027, China

A R T I C L E I N F O

Article history:
Received 28 March 2014
Received in revised form
16 May 2014
Accepted 31 May 2014
Available online 30 June 2014

Keywords:
Digital image correlation
Inverse compositional Gauss–Newton algorithm
Second-order shape function
Three-dimensional measurement

A B S T R A C T

The computational efficiency and measurement accuracy of the digital image correlation (DIC) have become more and more important in recent years. For the three-dimensional DIC (3D-DIC), these issues are much more serious. First, there are two cameras employed which increases the computational amount several times. Second, because of the differences in view angles, the must-do stereo correspondence between the left and right images is equivalently a non-uniform deformation, and cannot be weakened by increasing the sampling frequency of digital cameras. This work mainly focuses on the efficiency and accuracy of 3D-DIC. The inverse compositional Gauss–Newton algorithm (IC-GN^2) with the second-order shape function is firstly proposed. Because it contains the second-order displacement gradient terms, the measurement accuracy for the non-uniform deformation thus can be improved significantly, which is typically one order higher than the first-order shape function combined with the IC-GN algorithm (IC-GN^1), and 2 times faster than the second-order shape function combined with the forward additive Gauss–Newton algorithm (FA-GN^2). Then, based on the features of the IC-GN^1 and IC-GN^2 algorithms, a high-efficiency and high-accuracy measurement strategy for 3D-DIC is proposed in the end.

1. Introduction

Digital image correlation (DIC) is a non-interferometric and non-contacting optical metrology for full-field shape, motion and deformation measurements. Since its invention in the early 1980s [1,2], numerous studies have been performed by the scholars over the world [3,4], and significant improvements, such as basic principle, registration accuracy, computational efficiency and application fields have been achieved. It has become the most popular and powerful technique in experiment mechanics, and has been widely applied in various scientific and industrial fields [5–11].

In recent years, research on DIC is mostly focused on the computational efficiency and measurement accuracy. For the topic of computational efficiency, there are always tens of thousands grid points must be analyzed even in a single deformed image. With the development of digital cameras, the number of grid points would keep increasing year by year. Moreover, there are usually tens of thousands of deformed images recorded in the measurements, such as in a dynamic testing or in a real-time motion tracking. The computational cost of DIC therefore is generally considered to be very huge. A lot of achievements have been done to improve the computational efficiency of DIC [12–15]. As a typical DIC method, the forward additive Gauss–Newton (FA-GN) algorithm combining with the robust Zero-mean Normalized Sum of Squared Differences (ZNSSD) criterion is commonly used [16–18]. However the Hessian matrix of this method must be calculated and inverted in each iteration. As an equivalent but more efficient strategy [19,20], the inverse compositional Gauss–Newton (IC-GN) algorithm combining with ZNSSD criterion has been estimated [21]. However, both the IC-GN and FA-GN algorithms are actually at the same level of accuracy, the sub-pixel registration algorithm remains a key issue, especially for the non-uniform deformation.

In general, the DIC method can be classified broadly as either two-dimensional DIC (2D-DIC) [22] or three-dimensional DIC (3D-DIC) [23]. 2D-DIC employs just a single camera. It is only valid for the in-plane deformation. The measurement accuracy is very susceptible to the out-of-plane displacement [24]. To overcome the limitations of 2D-DIC, 3D-DIC based on the principle of binocular stereovision has been developed. By employing two synchronized cameras, 3D-DIC can measure not only the 3D shape but also the three displacement components of specimen surfaces. Namely, both the in-plane and out-of-plane deformations can be determined simultaneously. Therefore, 3D-DIC is commonly considered to be more accurate and practical than 2D-DIC.

It is worthy to note that although there are many advantages, the issues about the computational efficiency and measurement

---

* Corresponding authors.
E-mail addresses: chteng@ustc.edu.cn (T. Cheng), zhangqc@ustc.edu.cn (Q. Zhang).

http://dx.doi.org/10.1016/j.optlaseng.2014.05.013
0143-8166/

accuracy in 3D-DIC are much more serious than 2D-DIC. Firstly, because there are two cameras employed, the computational amount of 3D-DIC is approximately three times heavier than 2D-DIC. Secondly, the angle of the two cameras usually ranges from 25° to 65° in the practical implementations of 3D-DIC. Due to the differences in view angles, the left and right images recorded at the same time have obvious differences, which cannot be eliminated by increasing the sampling frequency of digital cameras. For example, the deformation variation in a single subset (with the subset size of 49 pixels) is up to 1.4% when the angle between the left and right cameras is about 40° in typical. Therefore, the must-do stereo correspondence between the left and right images in 3D-DIC is equivalently a non-uniform deformation, and cannot be weakened.

In this work, the authors have focused on the efficiency and accuracy of 3D-DIC. After conclusion some typical DIC methods, including the widely used FA-GN algorithms with first-order and second-order shape function (FA-GN^1, FA-GN^2 [25,26]), and the high-efficiency IC-GN algorithm with first-order shape function (IC-GN^1), Section 3 presents a new IC-GN algorithm with second-order shape function (IC-GN^2) to achieve the high-accuracy measurement of the non-uniform deformation. Section 4 presents the theoretical and experimental validations of this proposed method. Based on the different features of the IC-GN^1 and IC-GN^2 algorithms, Section 5 presents a high-efficiency and high-accuracy strategy for 3D-DIC. Section 6 presents concluding remarks.

2. DIC method using FA-GN algorithm

Fig. 1 schematically shows a typical DIC method using the FA-GN algorithm, where $\mathbf{W}(x,y;\mathbf{p})$ is the shape function (or named warp function) with a parameter vector $\mathbf{p}$ to describe the position and shape of the target subset relative to the original square reference subset. The subscript 1 and 2 denote whether the first-order or second-order shape function is employed. The ZNSSD criterion is usually performed to evaluate the similarity between the reference and target subsets. In each iteration, the current estimate of the target subset is compared with the reference subset to solve for the parameter increment $\Delta\mathbf{p}$, which is subsequently added to the parameter vector $\mathbf{p}$ to update the current estimate (namely, $\mathbf{p}=\mathbf{p}+\Delta\mathbf{p}$). The ZNSSD criterion thus can be described as

$$C_{\mathrm{ZNSSD}}(\Delta\mathbf{p})=\sum_{y=-M}^{M}\sum_{x=-M}^{M}\left\{\frac{f(\mathbf{W}(x,y;0))-\bar{f}}{f_s}-\frac{g(\mathbf{W}(x,y;\mathbf{p}+\Delta\mathbf{p}))-\bar{g}}{g_s}\right\}^2 \quad (1)$$

$$\mathbf{H}=\sum_{y=-M}^{M}\sum_{x=-M}^{M}\left\{\left(\nabla g\frac{\partial\mathbf{W}}{\partial\mathbf{p}}\right)^T\left(\nabla g\frac{\partial\mathbf{W}}{\partial\mathbf{p}}\right)\right\} \quad (2)$$

where f and g denote the gray levels at the point (x,y) of the reference and target subsets, $\bar{f}$and $\bar{g}$ denote the mean intensity values of the reference and target subsets, $M$is the half width of the subset, $f_s=\sqrt{\sum_{y=-M}^{M}\sum_{x=-M}^{M}[f(x,y)-\bar{f}]^2}$ and $g_s=\sqrt{\sum_{y=-M}^{M}\sum_{x=-M}^{M}[g(x',y')-\bar{g}]^2}$, $\mathbf{H}$is the Hessian matrix.

The first-order and second-order shape functions can be described respectively as:

$$\mathbf{W_1}(x,y;\mathbf{p_1})=\begin{bmatrix}x'\\y'\end{bmatrix}=\begin{bmatrix}1+u_x & u_y & u\\ v_x & 1+v_y & v\end{bmatrix}\begin{bmatrix}x\\y\\1\end{bmatrix}$$

$$\mathbf{p_1}=(u,u_x,u_y,v,v_x,v_y)^T \quad (3)$$

$$\mathbf{W_2}(x,y;\mathbf{p_2})=\begin{bmatrix}x'\\y'\end{bmatrix}=\begin{bmatrix}\frac{1}{2}u_{xx} & u_{xy} & \frac{1}{2}u_{yy} & 1+u_x & u_y & u\\ \frac{1}{2}v_{xx} & v_{xy} & \frac{1}{2}v_{yy} & v_x & 1+v_y & v\end{bmatrix}\begin{bmatrix}x^2\\xy\\y^2\\x\\y\\1\end{bmatrix}$$

$$\mathbf{p_2}=(u,u_x,u_y,u_{xx},u_{xy},u_{yy},v,v_x,v_y,v_{xx},v_{xy},v_{yy})^T \quad (4)$$

3. DIC method using IC-GN algorithm

Note that the Hessian matrix in the FA-GN algorithm must be calculated and inverted in each iteration, which seriously reduces the computational efficiency. Therefore, as shown in Fig. 2, the IC-GN algorithm combined with ZNSSD criterion has been proposed. In each iteration, the incremental warp $\mathbf{W}(x,y;\Delta\mathbf{p})$ is firstly exerted to the reference subset rather than the target subset, and subsequently inverted and composed with the current estimate $\mathbf{W}(x,y;\mathbf{p})$ to update the target subset:

$$\mathbf{W}(x,y;\mathbf{p})=\mathbf{W}(x,y;\mathbf{p})\,\mathbf{W}^{-1}(x,y;\Delta\mathbf{p}). \quad (5)$$

The ZNSSD criterion thus can be described as

$$C_{\mathrm{ZNSSD}}(\Delta\mathbf{p})=\sum_{y=-M}^{M}\sum_{x=-M}^{M}\left\{\frac{f(\mathbf{W}(x,y;\Delta\mathbf{p}))-\bar{f}}{f_s}-\frac{g(\mathbf{W}(x,y;\mathbf{p}))-\bar{g}}{g_s}\right\}^2. \quad (6)$$

To solve this equation, a first-order Taylor expansion with respect to $\Delta\mathbf{p}$ can be performed. This yields:

$$C_{\mathrm{ZNSSD}}(\Delta\mathbf{p})=\sum_{y=-M}^{M}\sum_{x=-M}^{M}\left\{\frac{f(\mathbf{W}(x,y;0))+\nabla f(\partial\mathbf{W}/\partial\mathbf{p})\Delta\mathbf{p}-\bar{f}}{f_s}-\frac{g(\mathbf{W}(x,y;\mathbf{p}))-\bar{g}}{g_s}\right\}^2 \quad (7)$$

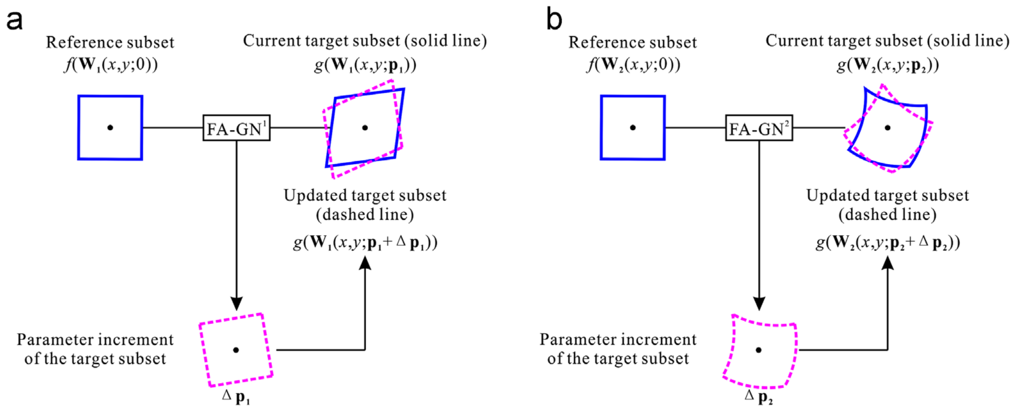

Fig. 1. Typical DIC method using the FA-GN algorithm with (a) the first-order shape function (FA-GN^1) and (b) the second-order shape function (FA-GN^2).

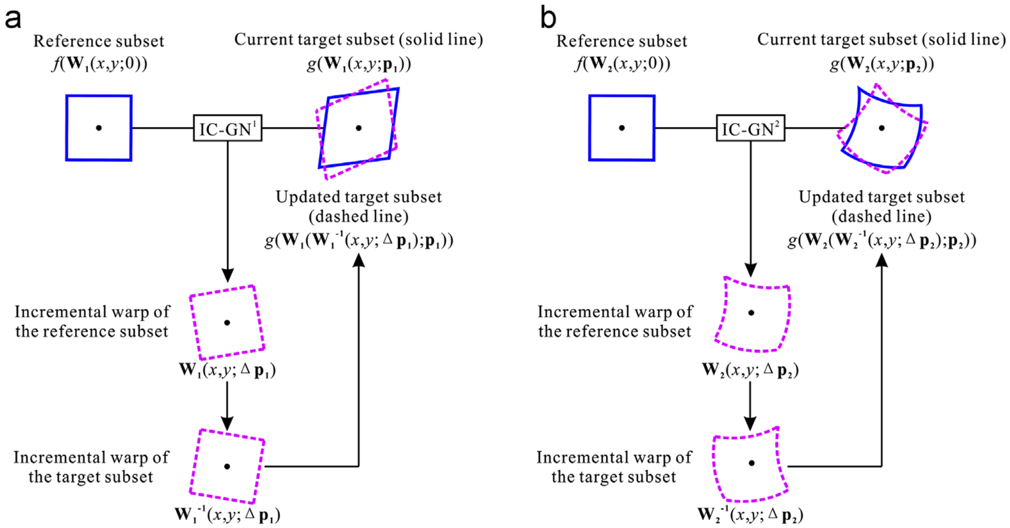

Fig. 2. DIC method using the IC-GN algorithm with (a) the first-order shape function (IC-GN^1) and (b) the second-order shape function (IC-GN^2).

where $\nabla f = ((\partial f/\partial x),(\partial f/\partial y))$ is the gradient of the reference subset. The solution of this least-squares problem is:

$$\Delta\mathbf{p} = -\mathbf{H}^{-1}\sum_{y=-M}^{M}\sum_{x=-M}^{M}\left\{\left(\nabla f\frac{\partial\mathbf{W}}{\partial\mathbf{p}}\right)^{\mathrm{T}}\left[f(\mathbf{W}(x,y;0)) - \bar{f} - \frac{f_s}{g_s}g(\mathbf{W}(x,y;\mathbf{p})) + \frac{f_s}{g_s}\bar{g}\right]\right\}. \tag{8}$$

$$\mathbf{H} = \sum_{y=-M}^{M}\sum_{x=-M}^{M}\left\{\left(\nabla f\frac{\partial\mathbf{W}}{\partial\mathbf{p}}\right)^{T}\left(\nabla f\frac{\partial\mathbf{W}}{\partial\mathbf{p}}\right)\right\}. \tag{9}$$

Note that the Hessian matrix in the IC-GN algorithm only depends on the reference subset and remains constant in each iteration. Namely there is no need to repeatedly estimate both the gradient of the target subset and the Hessian matrix. Therefore, the IC-GN algorithm is much more efficient than the FA-GN algorithm.

According to Eq. (5), the shape function applied in the IC-GN algorithm must be invertable and has the same form before and after update. For the first-order shape function, as shown in Fig. 2(a), it changes to a homogeneous form to meet these requirements:

$$\mathbf{W_1}(x,y;\mathbf{p_1}) = \begin{bmatrix} x' \\ y' \\ 1 \end{bmatrix} = \begin{bmatrix} 1+u_x & u_y & u \\ v_x & 1+v_y & v \\ 0 & 0 & 1 \end{bmatrix}\begin{bmatrix} x \\ y \\ 1 \end{bmatrix}. \tag{10}$$

Because the first-order shape function only allows the translation, rotation, normal strain, shear strain and their combinations of the target subset. Namely it can just depict the uniform deformation, and is not much suitable for the non-uniform deformation. Unfortunately, in fact, DIC often deals with relatively non-uniform deformations in many practical applications such as in fracture mechanics. It is worthy to note that the non-uniform deformation in 2D-DIC can be weakened by increasing the sampling frequency of digital camera, but the non-uniform deformation in 3D-DIC induced by the differences in view angles cannot be eliminated. Namely, the must-do stereo correspondence between the left and right images in 3D-DIC is an equivalent non-uniform deformation, and cannot be weakened. Therefore, in order to improve the measurement accuracy of the non-uniform deformation in 3D-DIC, the second-order shape function must be applied [26]. However, the simple operation in Eq. (10) cannot make the second-order shape function meet the requirements of IC-GN algorithm. For this reason, this paper proposed a new IC-GN algorithm with a second-order shape function (shown in Fig. 2 (b)). At first, the form of second-order shape function is expanded according to Eq. (4). The new components of the shape function can be derived as

$$\begin{aligned} x'^2 &= (1+S_1)\cdot x^2 + S_2\cdot xy + S_3\cdot y^2 + S_4\cdot x + S_5\cdot y + S_6 + o(h^2) \\ x'y' &= S_7\cdot x^2 + (1+S_8)\cdot xy + S_9\cdot y^2 + S_{10}\cdot x + S_{11}\cdot y + S_{12} + o(h^2) \\ y'^2 &= S_{13}\cdot x^2 + S_{14}\cdot xy + (1+S_{15})\cdot y^2 + S_{16}\cdot x + S_{17}\cdot y + S_{18} + o(h^2) \end{aligned} \tag{11}$$

where $S_1\cdots S_{18}$ are the functions of the parameter vector $\mathbf{p_2}$.

$$\begin{array}{ll} S_1 = 2u_x + u_x^2 + uu_{xx} & S_2 = 2uu_{xy} + 2(1+u_x)u_y \\ S_3 = u_y^2 + uu_{yy} & S_4 = 2u(1+u_x) \\ S_5 = 2uu_y & S_6 = u^2 \\ S_7 = \frac{1}{2}[vu_{xx} + 2(1+u_x)v_x + uv_{xx}] & S_8 = u_yv_x + u_xv_y + vu_{xy} + uv_{xy} + v_y + u_x \\ S_9 = \frac{1}{2}[vu_{yy} + 2u_y(1+v_y) + uv_{yy}] & S_{10} = v + vu_x + uv_x \\ S_{11} = u + vu_y + uv_y & S_{12} = uv \\ S_{13} = v_x^2 + vv_{xx} & S_{14} = 2vv_{xy} + 2v_x(1+v_y) \\ S_{15} = 2v_y + v_y^2 + vv_{yy} & S_{16} = 2vv_x \\ S_{17} = 2v(1+v_y) & S_{18} = v^2 \end{array} \tag{12}$$

The shape function then can be extended to a second-order form.

$$\mathbf{W_2}(x,y;\mathbf{p_2}) = \begin{bmatrix} x'^2 \\ y'^2 \\ x'y' \\ x' \\ y' \\ 1 \end{bmatrix} = \begin{bmatrix} 1+S_1 & S_2 & S_3 & S_4 & S_5 & S_6 \\ S_7 & 1+S_8 & S_9 & S_{10} & S_{11} & S_{12} \\ S_{13} & S_{14} & 1+S_{15} & S_{16} & S_{17} & S_{18} \\ \frac{1}{2}u_{xx} & u_{xy} & \frac{1}{2}u_{yy} & 1+u_x & u_y & u \\ \frac{1}{2}v_{xx} & v_{xy} & \frac{1}{2}v_{yy} & v_x & 1+v_y & v \\ 0 & 0 & 0 & 0 & 0 & 1 \end{bmatrix}\begin{bmatrix} x^2 \\ xy \\ y^2 \\ x \\ y \\ 1 \end{bmatrix}. \tag{13}$$

4. Validation of IC-GN^2

To quantitatively compare the efficiency and accuracy of the proposed DIC method using IC-GN^2 algorithm with the regular DIC method using the FA-GN^1, FA-GN^2, and IC-GN^1 algorithms, theoretical and experimental validations have been utilized in this study. All the algorithms were implemented using C++ language and tested on the PMLAB DIC-3D platform (Intel® Core™ i5-3450 CPU with 3.10 GHz and Kingston 1333 MHz DDR3 RAM). The generalized bicubic spline interpolation scheme is used to reconstruct sub-pixel intensity and gradient. The convergence condition is $||\Delta\mathbf{p}|| = ||\mathbf{p}^{n+1} - \mathbf{p}^{n}|| \le 10^{-3}$. For the first-order and second-order shape function, $||\Delta\mathbf{p}||$ is described below.

$$||\Delta\mathbf{p}_1|| = [(\Delta u)^2 + (\Delta u_x \times M)^2 + (\Delta u_y \times M)^2 + (\Delta v)^2 + (\Delta v_x \times M)^2 + (\Delta v_y \times M)^2]^{1/2}. \tag{14}$$

$$\begin{aligned}||\Delta\mathbf{p}_2|| = \Big[&(\Delta u)^2 + (\Delta u_x \times M)^2 + (\Delta u_y \times M)^2 \\ &+ \left(\tfrac{1}{2}\Delta u_{xx} \times M^2\right)^2 + (\Delta u_{xy} \times M^2)^2 + \left(\tfrac{1}{2}\Delta u_{yy} \times M^2\right)^2 \\ &+ (\Delta v)^2 + (\Delta v_x \times M)^2 + (\Delta v_y \times M)^2 \\ &+ \left(\tfrac{1}{2}\Delta v_{xx} \times M^2\right)^2 + (\Delta v_{xy} \times M^2)^2 + \left(\tfrac{1}{2}\Delta v_{yy} \times M^2\right)^2\Big]^{1/2}\end{aligned} \tag{15}$$

4.1. Numerical simulations

Fig. 3 shows the reference speckle image generated by a computer program [27]. There are totally 100,000 speckles with 1 pixel radius in the 500 × 500 pixels image. The yellow rectangle marks the region of interest (ROI) for the correlation operation. The purple rectangle marks the region of a single subset. The distribution of the self-correlation coefficient of ZNSSD along the x-axis with a radius of 20 pixels is shown in Fig. 3(b).

Two sets of deformed images are generated by applying the following deformation parameters to the reference image.

$$x' - x = U(x) = bT\ \sin\left(\frac{2\pi x}{T}\right),\quad T = 250,\ b = 0.001,\ 0.002,\ \cdots,\ 0.01 \tag{16}$$

$$\begin{bmatrix}\alpha x' \\ \alpha y' \\ \alpha\end{bmatrix} = \begin{bmatrix}1 & 0 & 0 \\ 0 & 1 & 0 \\ p & 0 & 1\end{bmatrix}\begin{bmatrix}x \\ y \\ 1\end{bmatrix},\quad p = 6\times10^{-5},\ 7\times10^{-5},\ \ldots,\ 15\times10^{-5} \tag{17}$$

The upper equation defines a sinusoidal non-uniform deformation field where $b$and T denote the amplitude and period of the displacement. The maximum deformation ($\varepsilon_{max} = (\partial u/\partial x)_{max} = 2\pi b$) ranges from 0.62% to 6.28%. The lower equation defines a plane-to-plane homography. In 3D-DIC, the left and right cameras view the specimen from different angles. The transformation between the left and right images is generally considered as a plane-to-plane homography [3]. If the digital cameras with 50 mm lenses and 10 μm pixel size are employed, the corresponding focal length is equal to 5000 pixels, and the angle between the left and right cameras ($\theta = 2\tan^{-1}(fp/2)$) ranges from 17° to 41°.

The reference image was meshed uniformly with a grid step of 3 pixels. All the grid points in the ROI are calculated using the FA-GN^1, FA-GN^2, IC-GN^1 and IC-GN^2 algorithms. The calculation errors were analyzed statistically in the following aspects:

$$e_u = \frac{1}{N}\sum_{i=1}^{N}|u_{calc} - u_{real}|. \tag{18}$$

$$\sigma_u = \sqrt{\frac{1}{N-1}\sum_{i=1}^{N}(|u_{calc} - u_{real}| - e_u)^2}. \tag{19}$$

where u_{calc} is the estimated displacement, u_{real} is the real displacement, N is the amount of grid points, e_u is the mean bias error of the calculated displacement along the x-axis, and σ_u is the standard deviation error of the calculated displacement along the x-axis.

Based on the two generated image sets, the calculated displacement errors (e_u,σ_u) and computation speed of the four algorithms are shown in Figs. 4 and 5, respectively, as the functions of subset size and parameter b or p.

In Figs. 4(a, c) and 5(a, c), it can be easily seen that with the increase of deformation and subset size, both the mean bias error and the standard deviation error increase rapidly for the FA-GN^1 and IC-GN^1 algorithms, but almost remain constant for the FA-GN^2 and IC-GN^2 algorithms. This significant distinction is mainly caused by the shape function. Because the second-order shape function is employed, the measurement accuracy of the FA-GN^2 and IC-GN^2 algorithms is much higher than the FA-GN^1 and IC-GN^1 algorithms when dealing with the general sinusoidal deformation and plane-to plane homography.

In Figs. 4(b, d) and 5(b, d), it can be easily seen that for all the four algorithms, the computation speed decreases obviously with the increase of subset size, but almost remains constant with the increase of deformation parameters. If the same order shape function is employed, the inverse algorithms are faster than the forward algorithms. If the same match strategy (neither inverse nor forward) is employed, the algorithms using the first-order shape function is much faster than those using the second-order shape function.

For a typical subset size 49 × 49 pixels and sinusoidal deformation parameter b=0.005, which corresponds to the maximum non-uniform deformation 3.14%, the positional errors of the FA-GN^2 algorithm (0.0045 pixel) and the IC-GN^2 algorithm (0.00498 pixel) are one order smaller than the FA-GN^1 algorithm (0.04395 pixel) and the IC-GN^1 algorithm (0.04364 pixel). The computational speed of IC-GN^2 algorithm (1849 points/second) is about 2.1 times of the

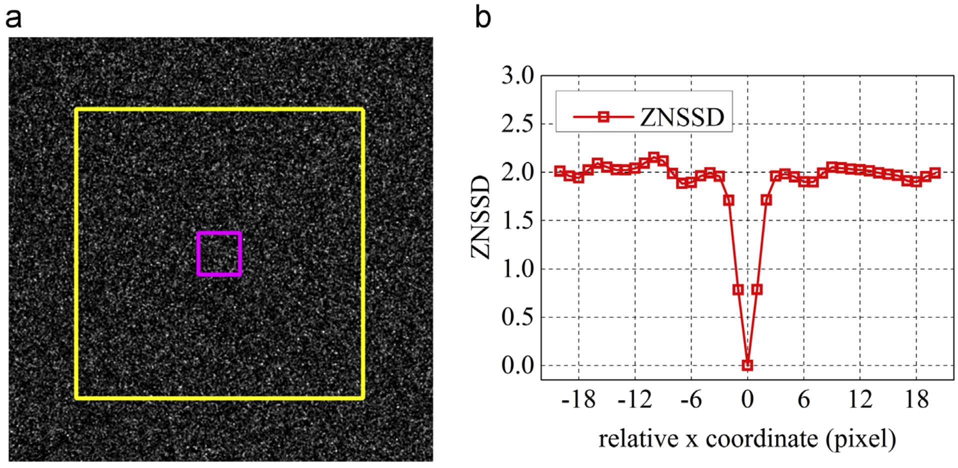

Fig. 3. (a) Reference speckle image generated by a computer program and (b) the distribution of the self-correlation coefficient of ZNSSD along the x-axis. (For interpretation of the references to color in this figure, the reader is referred to the web version of this article.)

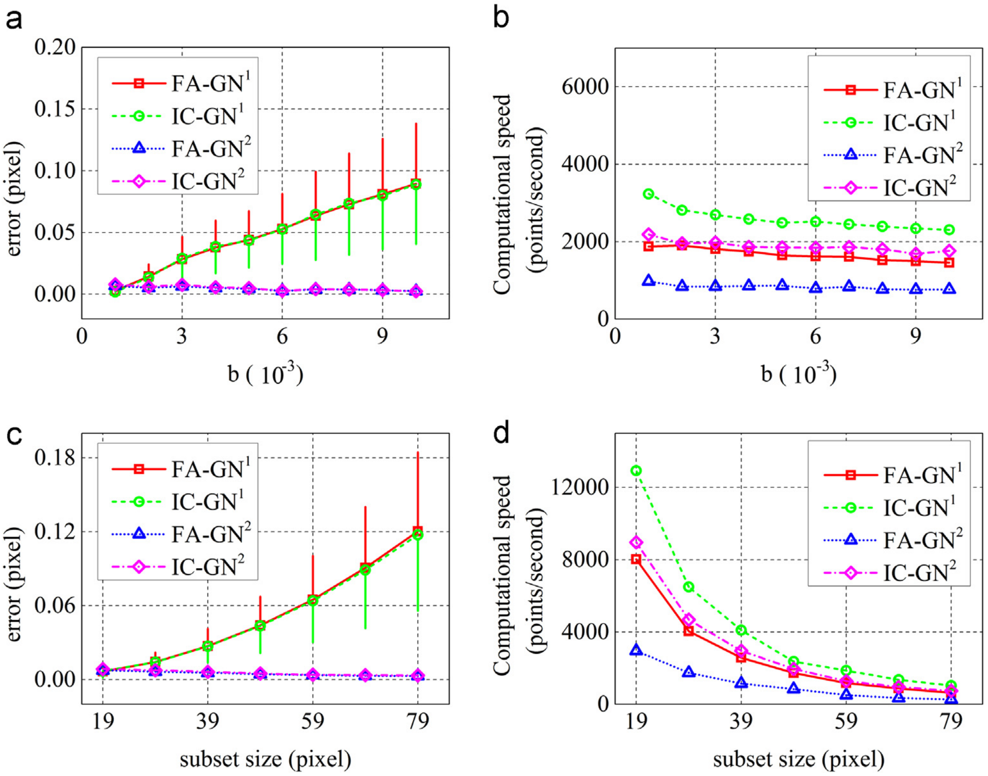

Fig. 4. Calculated displacement errors (e_u,σ_u) and computational speed of the four algorithms for the sinusoidal deformation image sets. (a, b) The errors and speed as a function of parameter b with a fixed subset size 49 × 49 pixels. (c, d) The errors and speed as a function of subset size with a fixed parameter $b = 0.005$.

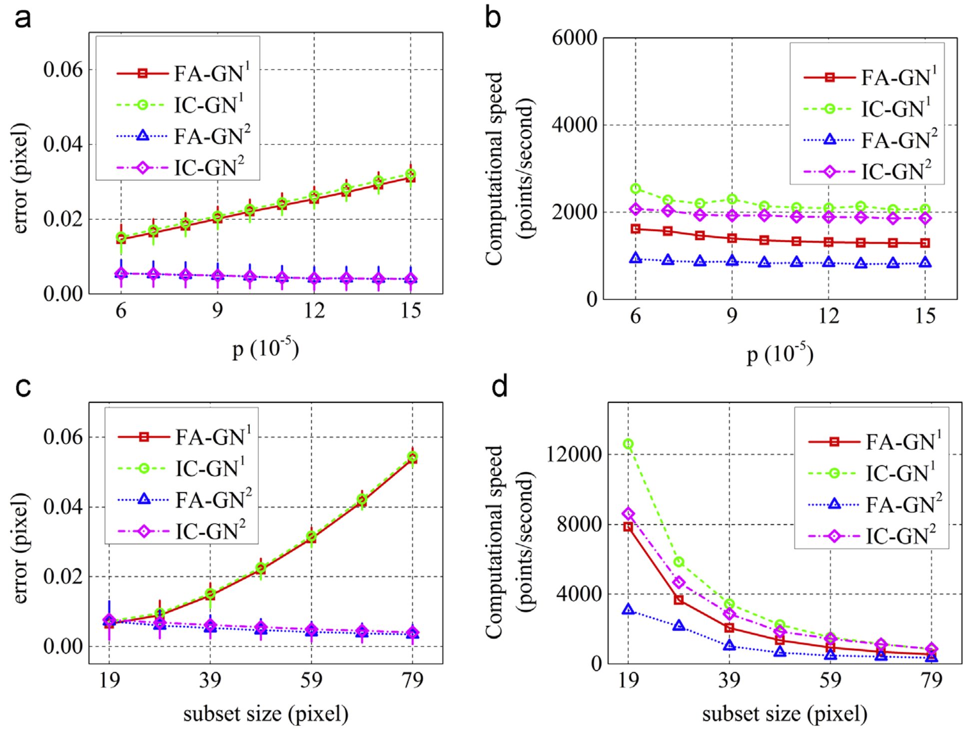

Fig. 5. Calculated displacement error (e_u,σ_u) and computational speed of the four algorithms for the homography image sets. (a, b) The errors and speed as a function of parameter p with a fixed subset size 49 × 49. (c, d) The errors and speed as a function of subset size with a fixed parameter $p = 0.0001$.

FA-GN2 algorithm (864 points/second) which has almost the same precision. And for a typical subset size 49 × 49 pixels and homography parameter $p = 1 \times 10^{-4}$, which corresponds to the angle about 28°, the positional errors of the FA-GN^2 algorithm (0.0047 pixel) and the IC-GN^2 algorithm (0.0047 pixel) are much smaller than the FA-GN^1 algorithm (0.022 pixel) and the IC-GN^1 algorithm

(0.02264 pixel). The computation speed of IC-GN^2 algorithm (1928 points/second) is about 2.3 times of the FA-GN^2 algorithm (833 points/second) which has almost the same precision.

These simulation results revealed that for the non-uniform deformation involved in 3D-DIC, the IC-GN^2 algorithm proposed in this study has the highest accuracy and the second fastest efficiency among all the four algorithms.

4.2. Experiments

A real bending experiment of a crack-board was performed to investigate the computational efficiency of the four algorithms. As is shown in Fig. 6, the left and right images with a resolution of 2448 × 2048 pixels and 8-bit depth were captured by two cameras from different angles. There are totally 29,798 grid points with the grid step of 7 pixels. The yellow rectangle marks the ROI.

Fig. 7(a) shows the ZNCC coefficient of all grid points calculated by the IC-GN^2 algorithm with the subset size of 49 × 49 pixels. The high ZNCC coefficient proves the correctness of the calculation, which is closed to the results by the other algorithms. Fig. 7(b) shows the comparison of computational efficiency among the four algorithms. Fig. 7(c, d) shows the calculated three-dimensional displacement field of V and strain field of eyy with the same reference image pair.

In Fig. 7(b), the computation speed decreases with the increase of subset size from 19 × 19 to 79 × 79 pixels. The computations determined experimentally are agreed with the simulation results. Due to the combination of the inverse strategy and the first-order shape function, the IC-GN^1 algorithm has the fastest efficiency, and is suitable for the uniform deformation. However, this algorithm may suffer from precision problem while handling non-uniform deformation. Due to the combination of the inverse strategy and the second-order shape function, the IC-GN^2 algorithm has the

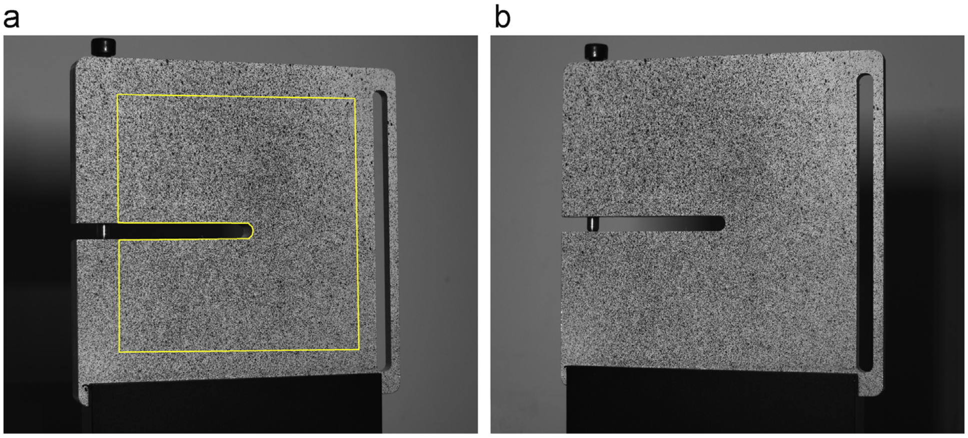

Fig. 6. (a) Left image captured by the left camera, the yellow rectangle marks the AOI and (b) right image captured by the right camera. (For interpretation of the references to color in this figure legend, the reader is referred to the web version of this article.)

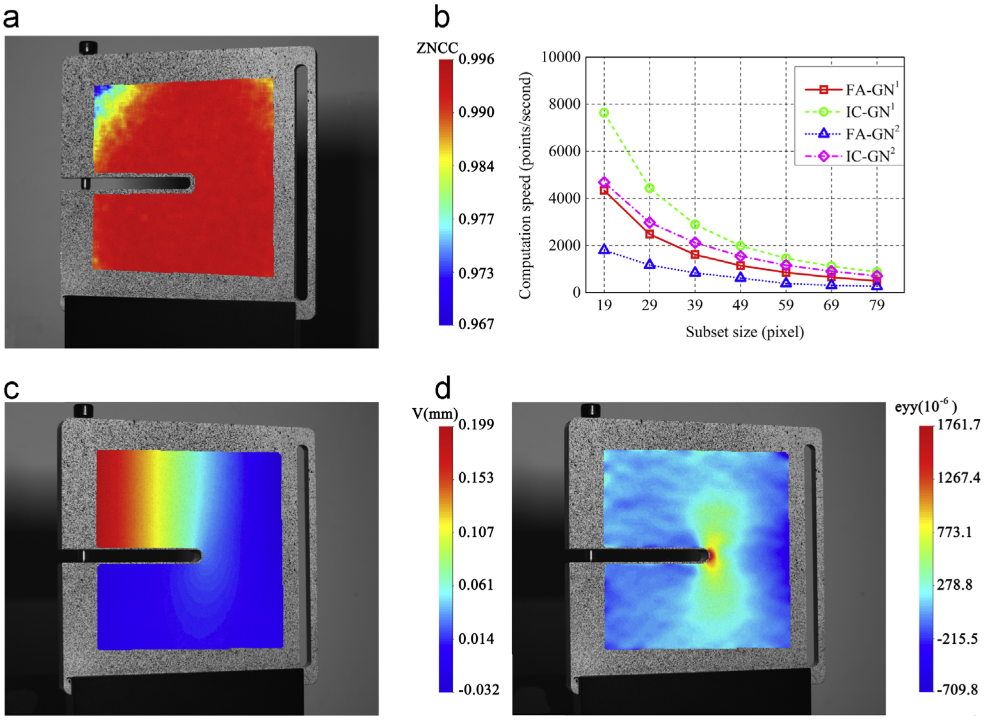

Fig. 7. Real bending experiment of a crack-board. (a) ZNCC coefficient of all grid points calculated by the IC-GN^2 algorithm, (b) computation speed as a function of subset size for the four algorithms, (c) calculated three-dimensional displacement field of V, and (d) strain field of eyy.

highest accuracy and second fastest efficiency, and is much more suitable for the non-uniform deformation.

5. Discussion

For the efficiency of the algorithms with forward additive (FA) strategy, the Hessian matrix must be calculated and inverted in each iteration. As a contrast, the algorithms with inverse compositional (IC) strategy evaluate the Hessian matrix only once. Therefore, the efficiency of the IC-GN algorithms is much higher than the FA-GN algorithms.

For the accuracy issue, the first-order shape function assumes that the deformation of the subset only contains translation, rotation and uniform strain, and can just depict the uniform deformation. As a contrast, the second-order shape function contains the second-order displacement gradient terms, and it is considered that the subset may suffer from non-uniform deformation. Therefore, the accuracy of the FA-GN^2 and IC-GN^2 algorithms is much higher than the FA-GN^1 and IC-GN^1 algorithms when dealing non-uniform deformation.

As is shown in Fig. 8, for a flat surface, when the angle between the left and right cameras is about 40° in typical, the deformation in the subset is theoretically non-uniform (described by the black curve) with a variation up to 1.4%, and it will be more serious for a curve surface. The strain result of IC-GN^1 algorithm is a constant about 0. As a contrast, the result of IC-GN^2 algorithm is more close to the theoretical value due to the nature of shape function.

5.1. High-efficiency and high-accuracy strategy for 3D-DIC

Actually, in 3D-DIC, because of the differences in view angles, the image pairs captured by the left and right cameras always have obvious differences. The must-do stereo correspondence between the left and right images in 3D-DIC is an equivalent non-uniform deformation, and cannot be weakened. Therefore, the stereo correspondences between the left and right images must employ the IC-GN^2 algorithm for the high-accuracy of the measurement (shown as the red dashed lines in Fig. 9). For the correlations among the left or right image sequence, there is generally only uniform deformation (note that the non-uniform deformation among the left or right image sequence can be weakened by increasing the sampling frequency of digital camera), the IC-GN^1 algorithm is enough to the measurement accuracy (shown as the blue solid lines in Fig. 9).

Therefore, there are probably three kinds of strategies for the correlations in 3D-DIC. The first strategy, as is shown in Fig. 9(a),

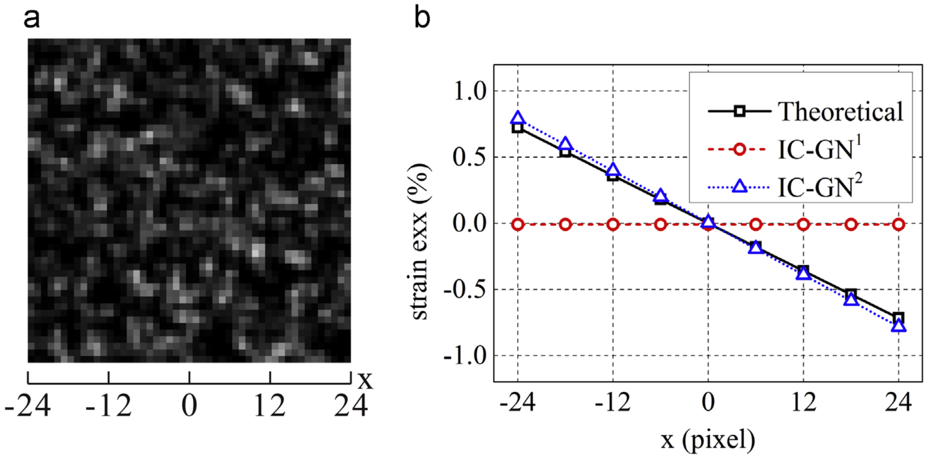

Fig. 8. Strain exx distribution along the *x*-axis in a single subset with homography deformation. (a) Speckle image of the subset and (b) strain exx as a function of *x* position in the subset.

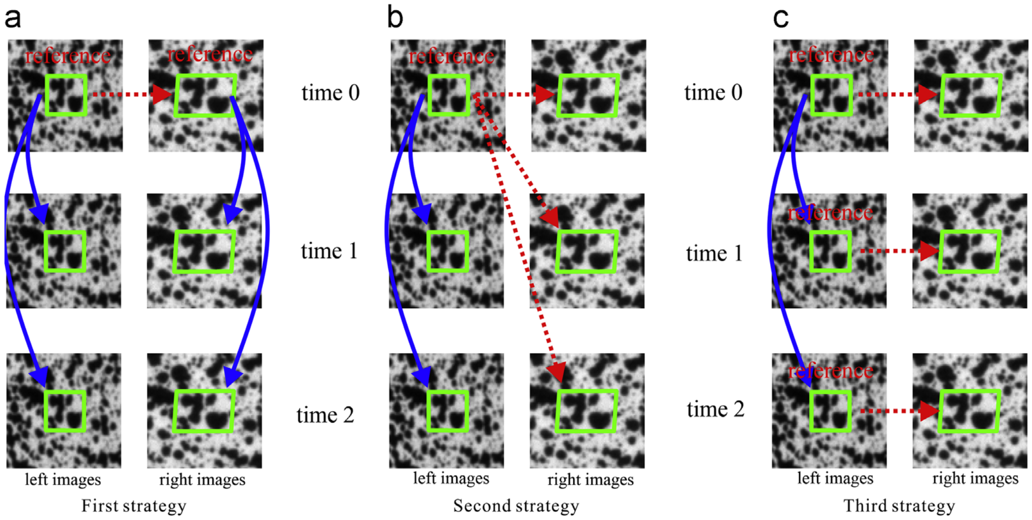

Fig. 9. Three kinds of strategies for the correlations in 3D-DIC. The red dashed lines indicate the stereo correspondence using IC-GN^2 algorithm and the blue lines indicate the correlation using IC-GN^1 algorithm. (For interpretation of the references to color in this figure legend, the reader is referred to the web version of this article.)

compares the left to the right image only once, namely the IC-GN^2 algorithm just performs in the initial stereo pair. After this point, succeeding left images are compared to the left reference using the IC-GN^1 algorithm, and succeeding right images are compared to the right reference using the IC-GN^1 algorithm too. The second strategy, as is shown in Fig. 9(b), uses left stereo reference, namely both the left and right images from any point in the sequence are always compared to the left reference image. The correlations of the left images should employ the IC-GN^1 algorithm, and the correlations of the right images should employ the IC-GN^2 algorithm. The third strategy, as is shown in Fig. 9(c), uses current left image, namely all left images from any point are always compared to the left reference image using the IC-GN^1 algorithm, and the right image from any point is always compared to the current left image using the IC-GN^2 algorithm

It can be easily seen that: the IC-GN^2 algorithm performed only once in the first strategy, therefore it is the best choice for the high-efficiency and high-accuracy measurement in 3D-DIC.

6. Conclusion

This study mainly focused on the efficiency and accuracy of 3D-DIC. Because the must-do stereo correspondence between the left and right images is an equivalent non-uniform deformation, and cannot be weakened, a new IC-GN algorithm with second-order shape function (IC-GN^2) is firstly proposed to achieve the high-accuracy measurement of the non-uniform deformation. The repetitive estimation of the Hessian matrix in each iteration has been eliminated, and the second-order shape function for the IC-GN algorithm has been derived. The theoretical and experimental validations have been utilized to compare the efficiency and accuracy of the proposed IC-GN^2 algorithm with the regular FA-GN^1, FA-GN^2, and IC-GN^1 algorithms. The IC-GN2 algorithm has the highest accuracy and second fastest efficiency among all the four algorithms. Typically, the accuracy is about one order higher than the IC-GN^1 algorithm, and the efficiency is about 2 times of the FA-GN^2 algorithm. The IC-GN^1 algorithm has the fastest efficiency and the second highest accuracy.

Subsequently, based on the features of the IC-GN^1 and IC-GN^2 algorithms, a high-efficiency and high-accuracy measurement strategy for 3D-DIC is proposed. The IC-GN^2 algorithm performs only once in the initial stereo pair. After this point, succeeding left images are compared to the left reference using the IC-GN^1 algorithm, and succeeding right images are compared to the right reference still using the IC-GN^1 algorithm too.

Acknowledgments

The authors are grateful for financial support received from the National Natural Science Foundation of China under Grant nos. 11372300, 11332010 51271174, and 11102201 and the National Basic Research Program of China under Grant no. 2011CB302105.

References

[1] Peters WH, Ranson WF. Digital imaging techniques in experimental stress analysis. Opt Eng 1981;21:427–31.

[2] Chu TC, Ranson WF, Sutton MA, Peters WH. Applications of digital-image-correlation techniques to experimental mechanics. Exp Mech 1985;25:232–44.

[3] Sutton MA, Orteu JJ, Schreier HW. Image correlation for shape, motion and deformation measurements. New York, USA: Springer; 2009.

[4] Hild F, Roux S. Digital image correlation: from displacement measurement to identification of elastic properties – a review. Strain 2006;42:69–80.

[5] Zhang QC, Jiang ZY, Jiang HF, Chen ZJ, Wu XP. On the propagation and pulsation of Portevin-Le Chatelier deformation bands: an experimental study with digital speckle pattern metrology. Int J Plast 2005;21:2150–73.

[6] Wang M, Hu XF, Wu XP. Internal microstructure evolution of aluminum foams under compression. Mater Res Bull 2006;41:1949–58.

[7] Wang HW, Kang YL. Improved digital speckle correlation method and its application in fracture analysis of metallic foil. Opt Eng 2002;41:2793–8.

[8] Wang HW, Kang YL, Zhang ZF, Qin QH. Size effect on the fracture toughness of metallic foil. Int J Fract 2003;123:177–85.

[9] Kang YL, Zhang ZF, Wang HW, Qin QH. Experimental investigations of the effect of thickness on fracture toughness of metallic foils. Mater Sci Eng A 2005;394:312–9.

[10] Zhang ZF, Kang YL, Wang HW, Qin QH, Qiu Y, Li XQ. A novel coarse-fine search scheme for digital image correlation method. Measurement 2006;39:710–8.

[11] Yang FJ, He XY, Quan CG. Characterization of dynamic microgyroscopes by use of temporal digital image correlation. Appl Opt 2006;45:7785–90.

[12] Pan B, Li K. A fast digital image correlation method for deformation measurement. Opt Lasers Eng 2011;49:841–7.

[13] Pan B. Reliability-guided digital image correlation for image deformation measurement. Appl Opt 2009;48:1535–42.

[14] Vendroux G, Knauss WG. Submicron deformation field measurements: Part 2. Improved digital image correlation. Exp Mech 1998;38:86–92.

[15] Huang JY, Zhu T, Pan XC, Qin L, Peng XL, Xiong CY, et al. A high-efficiency digital image correlation method based on a fast recursive scheme. Meas Sci Technol 2010;21:035101.

[16] B Lucas, T Kanade. An iterative image registration technique with an application to stereo vision. In: Proceedings of the international joint conference on artificial intelligence; 1981. pp. 674–679.

[17] Bruck HA, McNeil SR, Sutton MA, Peters WH. Digital image correlation using Newton–Raphson method of partial differential correction. Exp Mech 1989;29:261–7.

[18] Pan B, Xie HM, Wang ZY. Equivalence of digital image correlation criteria for pattern matching. Appl Opt 2010;49:5501–9.

[19] S Baker, I Matthews. Equivalence and efficiency of image alignment algorithms. In: Proceedings of the IEEE computer society conference on computer vision and pattern recognition; 2001. pp. 1090–1097.

[20] Baker S, Matthews I. Lucas-Kanade 20 years on: a unifying framework. Int J Comput Vis 2004;56:221–55.

[21] Pan B, Li K, Tong W. Fast, robust and accurate digital image correlation calculation without redundant computations. Exp Mech 2013;53:1277–89.

[22] Pan B, Qian KM, Xie HM, Asundi A. Two-dimensional digital image correlation for in-plane displacement and strain measurement: a review. Meas Sci Technol 2009;20:062001.

[23] Orteu JJ. 3-D computer vision in experimental mechanics. Opt Lasers Eng 2009;47:282–91.

[24] Sutton MA, Yan JH, Tiwari V, Schreier HW, Orteu JJ. The effect of out-of-plane motion on 2D and 3D digital image correlation measurements. Opt Lasers Eng 2008;46:746–57.

[25] Lu H, Cary PD. Deformation measurements by digital image correlation: implementation of a second-order displacement gradient. Exp Mech 2000;40:393–400.

[26] Schreier HW, Sutton MA. Systematic errors in digital image correlation due to undermatched subset shape functions. Exp Mech 2002;42:303–10.

[27] Zhou P, Goodson KE. Subpixel displacement and deformation gradient measurement using digital image/speckle correlation (DISC). Opt Eng 2001;40:1613–20.